Polar Firn Properties in Greenland and Antarctica and Related Effects on Microwave Brightness Temperatures

Haokui Xu[1], Brooke Medley[2], Leung Tsang[1], Joel T. Johnson[3], Kenneth C. Jezek[4], Macro Brogioni[5], and Lars Kaleschke[6]

[1]Radiation Laboratory, Department of Electrical Engineering and Computer Science, University of Michigan, Ann Arbor, MI 48105, USA
[2]Cryospheric Sciences Laboratory, NASA Goddard Space Flight Center, Greenbelt, MD, 20771, USA
[3]ElectoScience Laboratory, The Ohio State University, Columbus, OH, 43212, USA
[4]Byrd Polar and Climate Research Center, School of Earth Sciences, The Ohio State University, Columbus, OH 43210, USA
[5]Carrara Institute of Applied Physics, CNR, Florence, 50019, Italy
[6]Alfred-Wegener-Institut Helmholtz-Zentrum für Polar- und Meeresforschung, 27570 Bremerhaven, Germany

Correspondence to: Haokui Xu (xuhaoku@umich.edu)

Abstract. In studying the mass balance of polar ice sheets, the fluctuation of the firn density near the surface is a major uncertainty. In this paper, we explore these variations at locations in the Greenland Ice Sheet and at the Dome C location in Antarctica. Borehole in situ measurements, Snow Radar echoes, microwave brightness temperatures, and modelling results from the Community firn model (CFM) are used. It is shown that firn density profiles can be represented using 3 processes: "long" and "short" length scale density variations and "refrozen layers". Consistency with this description is observed in the dynamic range of airborne 0.5-2 GHz brightness temperatures and Snow Radar echo peaks in measurements performed in Greenland in 2017. Based on these insights, a new analytical partially coherent model is implemented to explain the microwave brightness temperatures using the three scale description of the firn. Short and long scale firn processes are modelled as a 3D continuous random medium with finite vertical and horizontal correlation lengths as opposed to past 1D random layered medium descriptions. Refrozen layers are described as deterministic sheets with planar interfaces, with the number of refrozen layer interfaces determined by radar observations. Firn density and correlation length parameters used in forward modelling to match measured 0.5-2 GHz brightness temperatures in Greenland show consistency with similar parameters in CFM predictions. Model predictions also are in good agreement with multi-angle 1.4 GHz vertically and horizontally polarized brightness temperature measured by the SMOS satellite at DOME C, Antarctica. This work shows that co-located active and passive microwave measurements can be used to infer polar firn properties that can be compared with predictions of the CFM. In particular, 0.5-2 GHz brightness temperature measurements are shown to be sensitive to long scale firn density fluctuations with density standard deviations in the range 0.01-0.06 g/cm^3 and vertical correlation lengths of 6-20 cm.

1 Introduction

The mass balance of polar ice sheets is a major topic in the study of climate change. The most recent assessment of the mass balance of the Greenland and Antarctic Ice sheets confirmed a loss of ice to the ocean at a rate of 320 Gt/year, equivalent to 1 mm sea level rise per year since 2003 [Smith et al., 2020]. The quantification of uncertainty in ice-sheet volume change between NASA's first- and second-generation Ice, Cloud, and land Elevation Satellites (ICESat, ICESat-2) is a testament to the precision of these laser altimeters. For example, uncertainties for the grounded AIS and GrIS are currently ~5 and 3 km^3 yr-1, respectively, as compared to volume changes of -111 and -235 km^3 yr-1[Smith et al., 2020]. At present, the largest source of uncertainty in altimetric measurements of mass balance stems from the volume-to-mass conversion within which firn processes dominate [Smith et al., 2020, Shepherd et al., 2019].

When snow falls on the ice sheet, it slowly densifies into solid ice with increasing depth in a manner that is dependent on the pressure imparted by subsequent snowfall, the physical temperature, and any refreezing of infiltrated liquid water. The resulting transitional material is referred to as firn. Firn typically ranges in thickness from 10's to >100 meters over ice sheets (Ligtenberg et al., 2011; Kuipers Munneke et al., 2015). The density of the firn column at a given location varies in time in response to short and long time-scale variations. Because the material density of the firn column is much less than that of solid ice[Smith et al., 2020, Medely et al., 2022], its thickness variations often manifest as a much larger portion of the total column thickness change than ice dynamic change. For example, firn density profiles in depth show fluctuations due to yearly snowfalls [Stevens et al., 2020]. The fluctuation amplitude becomes smaller and more rapid as depth increases because of densification effects.

Because of the large spatiotemporal variations in firn column properties, it can be extremely difficult to measure at the spatial scales required to support detailed modelling efforts. In situ measurements of the firn depth-density profile exist sporadically across both ice sheets in time and space [Montgomery et al., 2018]. While these observations provide a snapshot of firn properties, direct evidence of their evolution through time at sufficient resolutions applicable to altimetry studies (seasonally) remains a major challenge. Modelling efforts have attempted to fill in some of these knowledge gaps [Li and Zwally,2011; Kuipers Munneke et al., 2015], but their ability to realistically simulate firn processes remains incompletely understood in the absence of the extensive in-situ observations.

Active and passive microwave sensors can also inform us about the scattering and emission properties of the firn over large scales (Koenig et al 2007; Brucker et al., 2010; Champollion et al., 2013, Medley et al., 2015); these properties are ultimately related to the physical properties of the firn. The strongest echoes in a radar echogram, for example, show the position of abrupt permittivity changes that usually correspond to the position of refrozen melt layers (Jezek and others, 1994; Zabel and others, 1995). Several studies have used active microwave remote sensing to track the internal stratigraphy (radar reflection horizons related to density contrasts) of the firn to infer spatiotemporal variations in snow accumulation rates [Medley et al.,

2013; 2014; Koenig et al., 2016; Dattler et al., 2019]. Although radar echoes are able to position internal firn layers, using the radar data only to quantitatively study firn densification remains challenging.

Passive microwave brightness temperature measurements in the range 0.5-2 GHz can also reflect the effects of internal density fluctuations [Brogioni et al, 2015; Tan et al, 2021;]. In our previous works[Yardim etal 20222], we have used UWBRAD to sense the subsurface temperature profile, in which case the reflections caused by firn density fluctuations are nuisance effects. Unlike radars which observe scattered powers only in the backscattered direction, radiometer brightness temperature observations are sensitive to scattering in all scattering directions within the firn as shown by Kirchhoff's Law[Tsang 2001].

In this paper, we use co-located Snow Radar echoes (acquired in Greenland during the Operation Ice Bridge Campaign 2017, [CReSIS. 2021]) and 0.5-2 GHz brightness temperature data (the latter collected by the Ultra-Wide Band Software Defined Radiometer (UWBRAD) in 2017) to quantitatively evaluate firn density fluctuations in the Greenland ice sheet. The ~~firn~~ firn density properties derived from microwave sensor data in Greenland are compared with simulated profiles from the Community Firn Model (CFM) since high resolution measurements are not available. The CFM simulated profiles are first evaluated by compared to in-situ measurements. A radiative transfer model with 3D density variation effects is implemented to interpret the measured brightness temperature. Unlike the one-dimensional stochastic profiles used in previously brightness temperature modelling studies [Tan et al 2015, Tan et al 2021], a horizontal correlation length, l_ρ, is introduced for the short (due to temporal effects) and long scale(due to yearly snow fall) processes to represent their variations in horizontal directions. This approach results in a continuous random medium description of the firn as opposed to the past stochastic layered medium description. "Refrozen layer" effects (high or low-density density discontinuities) also were not included in [Tan et al 2015, Tan et al 2021], but are included in this paper.

The model then shows the effects of the long scale and refrozen layers to be significant, while those of the short scale process are negligible, and the impact of the long scale process is shown to depend on the microwave frequency. The number of freezing layers and their positions used in the model are determined from Greenland radar echo data. The results also show that freezing layers introduce a frequency dependence in 0.5- 2 GHz brightness temperatures that differs from that of the long scale process.

The model developed also suggests a means for combining active and passive microwave measurements to sense properties of firn density profiles in areas lacking in situ measurements. The method first estimates the number and location of freezing layers using radar echo measurements. The impact of these layers is then removed (based on the partially coherent model), and properties of the long scale density fluctuations are estimated by matching model predictions to 0.5-2 GHz measured brightness temperatures. Results suggest that the long scale vertical correlation length can be estimated in this manner.

We also discuss the H and V brightness temperature measurements over DOME-C, Antarctica where the effects of melt event is considered insignificant. By modelling the density variation as 3D, the polarization dependence of the measurement can be explained. This indicates the ability of predicting V and H channel TB at off nadir directions

Formatted: Font color: Red

2. Method

2.1 Ultra-Wide Band software defined Radiometer (UWBRAD) and Snow Radar data

UWBRAD measures ice sheet 0.5-2GHz brightness temperatures in a nadir viewing geometry [Andrews etal 2015]. The cumulative effects of the temperature profile, density fluctuations, and the effects of refrozen layers are all included in the sensed brightness temperature. Two measurement flights are taken over Greenland in the year of 2016 and 2017. The 2016 flight path ended near Camp Century while the 2017 flight has a much longer patch which not only covers Camp Century but also NEEM and NGRIP.

The University of Kansas Snow Radar [Panzer., et al., 2010] included in Operation IceBridge campaigns operates over the 2–6.5 GHz frequency range. Because the corresponding 4.5 GHz bandwidth enables a 2 cm vertical resolution of firn echoes, snow radar data can help to characterize near-surface properties of the firn. Starting summer 2012, great melt events occur over the whole Greenland, creating refrozen layers in the firn. In particular, high dielectric contrast refrozen layers that extend over larger horizontal distances produce significant radar backscatter, enabling their characterization with radar measurements. Effects of these finite number of high frozen layers in the radiometer has never been included. The depths and number of refrozen layers within the firn can also be inferred based on the time delay of the associated radar echo. Radar measurements however are not optimal for sensing moderate density fluctuations within the firn because such fluctuations do not produce high backscattered power levels due to their low dielectric contrast.

To validate the potential utility of combined active and passive measurements of firn properties, locations one through four listed in Table 1~~Table 1~~ where Snow Radar and UWBRAD were nearly co-located over Greenland in 2017 were identified based on the 2017 flight paths shown in Figure 3. An X-ray tomography data near the first location compared with the radar echo to validate the existence of refrozen layers.

Overlapping location index (North to south)	Latitude	Longitude
1	77.266N	49.121W
2	76.563N	44.778W
3	76.168N	44.329W
4	75.535N	42.7948W

Table 1: Latitude and Longitude for crossover locations of 2017 UWBRAD and Snow Radar Measurements

Formatted: Font color: Red

Formatted: Font color: Red

Formatted: Font color: Red

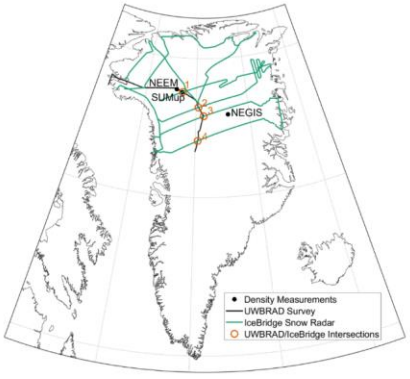

Figure 1 Flight paths of UWBRAD and Snow Radar in 2017.

2.2 The Conmmunity Firn model and In-situ measurements

Formatted: Font color: Red

The locations where active and passive measurements are both available is presented in figure 1. Although lots of in-situ measurements of the snow density is available, they are spread in a large spatial and temporal scale [Montgomery,etal (2018)]. Previous studies have shown that thermal emission at 0.5-2GHz is highly influenced by the density fluctuations in the range of centimetre scale. However, in-situ measurements are usually take on the scale of tens of centimetres which does not fit the need of characterizing the density statistics on the microwave scale. Thus, to evaluate the inferred the density fluctuations from microwave sensor data, we use the modelled firn profile as a reference.

Formatted: Font color: Red

We use the Community Firn Model v1.1.6 (CFM; Stevens et al., 2020, 2021) to simulate the firn column density profile at several locations across the ice sheet. The CFM was built as a resource to the glaciology community, and consists of a modular, open-source framework for Lagrangian modelling of several firn and firn-air related processes (Stevens et al 2020). CFM simulations are set up as detailed in Medley et al. (in Review) where the model is forced by a modified version of the MERRA-2 global atmospheric reanalysis (Gelaro et al., 2017) at 5-day temporal resolution. The only difference between the CFM simulations from Medley et al. (in Review) and those presented here is that a time-varying initial density ρ_0 of the firn column is introduced using the parameterization in Fausto et al. (2018): $\rho_0 = 362.1 + 2.78\,T_a$, where T_a is the atmospheric temperature in °C at each time step. When comparing CFM-generated density profiles with observations, we use the simulated profile that is most contemporaneous with the observations. For a detailed description of the CFM set up, see Medley et al. (in Review). The vertical density profile of the firn can be characterized by $\rho(z) = \rho_m(z) + \rho_f(z)$, where $\rho_m(z)$ is a mean profile that gradually increases with depth and $\rho_f(z)$ is a fluctuating profile which fluctuates around $\rho_m(z)$ and is characterized by standard deviation $\Delta\rho(z)$ and correlation length $l_z(z)$.

We selected 3 locations to compare in-situ measurements and CFM simulations. The first profile was collected at T41 (71.08N,37.92W) along the EGIG line by Morris [Morris and Wingham 2011] in 2004 using a neutron probe (Figure 1, left). Data were collected up to 13 meters below the surface at a vertical resolution of 1 cm, and clearly show significant fluctuations in density in the upper firn. The second profile and third profiles (Figure 2) are from a 2009 borehole measurement at the NEEM site [Ian Baker. 2012. NEEM Firn Core 2009S2 Density and Permeability] with a vertical resolution of ~90 cm and from a 2012 measurement at the NEGIS [Vallelonga et al., 2014] site having ~1 m increments. The goal is to evaluate whether the CFM simulation can provide a density fluctuation and a mean profile that are physical compared to the real world

2.3 Analytical Partially coherent model

To interpret the brightness temperature, an analytical partially coherent model is implemented. An illustration of ice sheet thermal emission problem is shown in Figure 2. A firn layer of thickness d_1 (region 1) exists near the ice sheet surface. The density of the firn layer is modelled as $\rho(\vec{r}) = \rho_m(z) + \rho_f(\vec{r})$ with $\rho_m(z)$ the mean density profile. Due to the great melt events starting in 2012, refrozen high density layers appear in the region which is typically considered as dry zone. The effects of these layers are also considered. The fluctuating profile is described as $\rho_f(\vec{r}) = \rho_{fs}(\vec{r}) + \rho_{fl}(\vec{r})$. Notice that the fluctuating profile varies in three dimensions and has two scales, short (ρ_{fs}) and long (ρ_{fl}). The real and imaginary parts of the microwave permittivity of the firn are related to the firn density using the models in [Matzler, Tiuri]. The correlation function for each scale of the fluctuating density is described by

$$(\Delta\varepsilon_{rf})^2 C(|\vec{r}-\vec{r}'|) = (\Delta\varepsilon_{rf}(z))^2 \exp(-\frac{|z-z'|}{l_z(z)}) \exp(-\frac{(x-x')^2+(y-y')^2}{l_\rho^2}) \quad \text{E.q.(1)}$$

in which $\Delta\varepsilon_{rf}(z)$ ~~$\Delta\varepsilon_{rf}(z)$~~ is the standard deviation, $l_z(z)$ is the permittivity vertical correlation length, and l_ρ is the horizontal correlation length. The correlation function is described as having a Gaussian form laterally and an exponential form vertically based on the model used in [Tsang 2001]. The exponential form for the vertical correlation function is adopted based on analyses showing similar properties for the firn density itself[Tsang 2001T]. Both $\Delta\varepsilon_{rf}(z)$ ~~$\Delta\varepsilon_{rf}$~~ and l_z are modelled as functions of depth due to the compaction of the firn, while l_ρ is modelled as independent of depth.

Below region 1, the main ice body can be multiple km thick with a temperature profile that varies in depth. Thermal emission from the main ice body is calculated using the existing partially coherent model [Tan et al 2021] and the temperature profile obtained in [Yardim et al 2022]. The temperature in region 1 is modelled as a constant value T_0 . Although the top 10-20 m of firn experiences seasonal temperature changes, these variations have little effect on brightness temperatures at frequencies less than 2 GHz due to the limited emission directly from the firn layer.

Formatted: Font color: Red

Formatted: Font color: Red

Field Code Changed

Field Code Changed

Applying the radiative transfer theory of microwave emission and scattering, the upward and downward propagating specific intensities $\vec{I}_u$ and $\vec{I}_d$ in region 1 satisfy

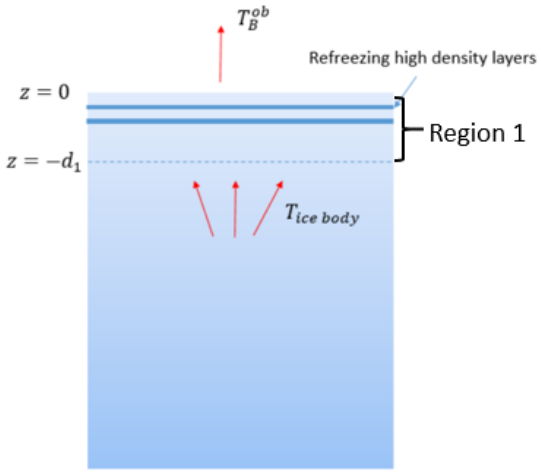

Figure 22 Thermal emission from an ice sheet

$$\cos\theta \frac{d}{dz}\vec{I}_u(\theta,z) = -\kappa_a(z)\vec{I}_u(\theta,z) - \overline{\overline{\kappa_s}}(\theta,z)\vec{I}_u(\theta,z) + \kappa_a(z)C\vec{T}_0 + \int_0^{2\pi}\sin\theta' d\theta' \overline{\overline{F}}(\theta,\theta',z)\vec{I}_u(\theta',z) + \int_0^{2\pi}\sin\theta' d\theta' \overline{\overline{B}}(\theta,\theta',z)\vec{I}_d(\theta',z)$$

$$-\cos\theta \frac{d}{dz}\vec{I}_d(\theta,z) = -\kappa_a(z)\vec{I}_d(\theta,z) - \overline{\overline{\kappa_s}}(\theta,z)\vec{I}_d(\theta,z) + \kappa_a(z)C\vec{T}_0 + \int_0^{2\pi}\sin\theta' d\theta' \overline{\overline{B}}(\theta,\theta',z)\vec{I}_u(\theta',z) + \int_0^{2\pi}\sin\theta' d\theta' \overline{\overline{F}}(\theta,\theta',z)\vec{I}_d(\theta',z) \quad \text{E.q.(2)}$$

with the boundary conditions:

$$\vec{I}_d(\theta, z=0) = \overline{\overline{r}}_{10}(\theta)\vec{I}_u(\theta, z=0)$$
$$\vec{I}_u(\theta, z=-d_1) = CT_2 \quad \text{E.q.(3)}$$

In the above equations, $\vec{I}_u$ and $\vec{I}_d$ are 2 x1 vectors in which the upper row is for vertical polarization and the lower row for horizontal polarization. $\kappa_a(z)$ is the absorption coefficient determined by the mean density profile while $\overline{\overline{\kappa_s}}(\theta,z)$ is the scattering coefficient due to the randomly fluctuating portion of the density profile. The phase matrices $\overline{\overline{F}}$ and $\overline{\overline{B}}$ couple specific intensities from other directions θ' into the direction of interest θ in the forward or backward propagating hemispheres. The boundary conditions specify that the firn-to-air interface at $z = 0$ is reflective with reflection coefficient $\overline{\overline{r}}_{10}(\theta)$ and that the compacted firn to ice interface at $z = -d_1$ with $d_1 = 100m$ is not reflective. An iterative approach is then used to solve the equations. Since the permittivity variation is small, the first order solution together with the zeroth order

Formatted: Font color: Red

solution provides sufficient accuracy. A detailed solution of the equations can be found in Appendix A. The method is partially coherent because the phase matrices are obtained using a coherent formulation of the continuous medium scattering problem.

High-density refrozen layers are included by incorporating their additional reflections as

$$T_b^{ob} = (1-r_{10})\frac{\lambda^2}{K}\frac{1}{\varepsilon'_{rm1}}(I_u{}^{(0)}(\theta=0,z=0)+I_u{}^{(1)}(\theta=0,z=0))\prod_n(1-r_n^{refrez}) \quad \text{E.q.(4)}$$

where $\prod_n(1-r_n^{refrez})$ accounts for the transmission from each layer. This multiplicative approach is reasonable because the microwave wavelength between 0.5~2GHz is larger than the typical layer thickness.

The resulting model captures coupling between scattering in different directions and polarizations through the phase matrices $\bar{\bar{F}}$ and $\bar{\bar{B}}$. The previous "random layer" 1D formulation of Tan et al 2021 captures neither of these effects.

3. Results

3.1 Firn density measurements at borehole sites and the associated CFM profiles

The high resolution profile(1cm resoltuion) at T41 enables an estimation the standard deviation $std(\rho)$ and correlation length l_z of the fluctuating profile every meter in depth (Tabel 2). The coarser profiles(~1m resoltuion) at Sites 2 and 3 do not allow such analysis, but information on the depth at which a "critical" density (i.e., 550 kg m^{-3}) is reached can be obtained.

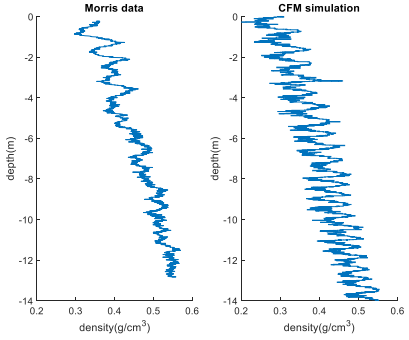

Figure 3: (left) Morris and Wingham, 2011 density profile measured near Summit station, Greenland, Summer 2004 (right) corresponding CFM model simulation

In Figure 3, the profiles from T41 high resolution measurements and CFM simulation is plotted. The standard deviation of density and its correlation length based on 1m profile is provide in Table 2. Both the in-situ and CFM profiles at T41 show small and fast variations superimposed on the larger but relatively slowly varying mean profile. One-meter density standard deviations ($std(\rho)$) in Table 1 for the neutron probe and CFM are comparable, with most of the values around 0.03 g/cm^3.

Formatted: Font color: Red

Vertical correlation lengths obtained both from the Morris' profile and the CFM simulation are <20 cm with mean values of 14.2 and 9.4cm, respectively. The results from CFM usually used to evaluate the mean firn density.

Depth(z)	Neutron Probe data		CFM	
	$std(\rho)(\frac{g}{cm^3})$	l_z(cm)	$std(\rho)(\frac{g}{cm^3})$	l_z(cm)
0	0.028	16	0.03	9.6
2	0.019	17	0.027	12
4	0.01	12	0.029	11
6	0.012	17	0.028	9
8	0.011	12	0.028	7.5
10	0.0086	11	0.023	7

Table 22: Estimated density standard deviations (std(ρ)) and correlation lengths (l_z) estimated using 1 m of data beginning at the specified depth for Summit Station, Greenland from Neutron Probe dataset of Morris and Wingham, 2011 and the CFM The comparison here is to show that 1. the CFM is not generating very large fluctuations ($std(\rho)$>$mean(\rho)$) since observed density profile shows a rms density of fluctuation smaller than the mean profile.2. The simulated profile is not changing too slow compared to the measurements. If the profile is changing too slow ($l_z\ CFM$>$2l_z measured$), this means that the simulated CFM profile is not able to characterize the density changes. This shows that CFM results are reasonable compared to measured data. The comparison here is performed for the statistics of "long scale" (l_z of several cm) which is mainly due to the yearly snow fall. The "short scale"(l_z <2cm), even we have seen the fluctuations in the profile, cannot be captured since the data resolution is comparable to the correlation length.

Site	Critical density depth: In-situ (m)	Critical density depth: CFM (m)
NEEM	15.8	14
NEGIS	18.11	18.13

Table 3: Estimated depth at which mean density profile reaches critical density value of 550 kg m-3 for NEEM and NEGIS In-situ Measurements and corresponding CFM simulations

Formatted: Font color: Red
Formatted: Font color: Red
Formatted: Font color: Red
Formatted: Font color: Red
Formatted: Font color: Red
Formatted: Font color: Red
Formatted: Font color: Red

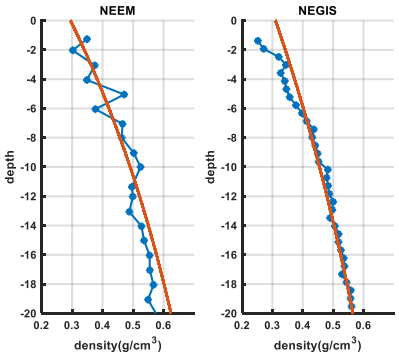

Figure 4: In-situ and CFM density profiles for the NEEM site In-situ and CFM density profiles (blue: ice core data, orange: fitted mean profile from CFM simulation) for the NEGIS site.

In figure 4, we show the ice core measurement of NEEM(left) and NEGIS(right) plotted together with the mean profile generated from CFM. We fit the ice core data with an exponential function of depth that was then extrapolated to find the depth at which the exponential function reached 550 kg m^{-3}. The resulting depths from NEEM and NEGIS and from the corresponding CFM simulations are shown in Table 3. Fig.4 shows reasonable agreement as observing the CFM simulated mean profile plotted together with the borehole measurements. The NEEM site shows a difference of 1.8m in the position of critical density, this is due to fitting the 2 stages of densities with a single exponential.

The results of this section suggest that the CFM, when run at a high time resolution, can produce firn density profiles that are in reasonable agreement with in-situ measurements. The mean profiles, as shown in the comparison, are in good agreement with the measurements.

3.2 refrozen layers in the upper frin region

As stated earlier, the great melt events creates refrozen layers in the "dry" zone of Greenland. In this section, we compare the Snow Radar echogram with the CFM simulated profiles. An X-ray tomography profile near location 1 collected in 2015[Montgomery,etal (2018)] is also compared with the radar echo. Figure 5~~Figure 4~~ plots three example radar echo profiles near location 1 in Figure 1 along with an echogram showing multiple profiles versus position along the flight path. Individual echo profiles show multiple significant backscatter peaks in the upper firn, but the echogram demonstrates that returns can fluctuate significantly from location to location. An average of radar echoes over a 1 km distance surrounding each site was therefore performed. CFM profile simulations also account only for large-scale climate properties in simulating firn profiles, so that a spatial average of radar measurements is also reasonable, and UWBRAD measurements also correspond to a footprint of 1 km diameter.

Formatted: Font color: Red

Formatted: Font color: Red

Formatted: Font color: Red

Formatted: Font color: Red

Formatted: Font color: Red

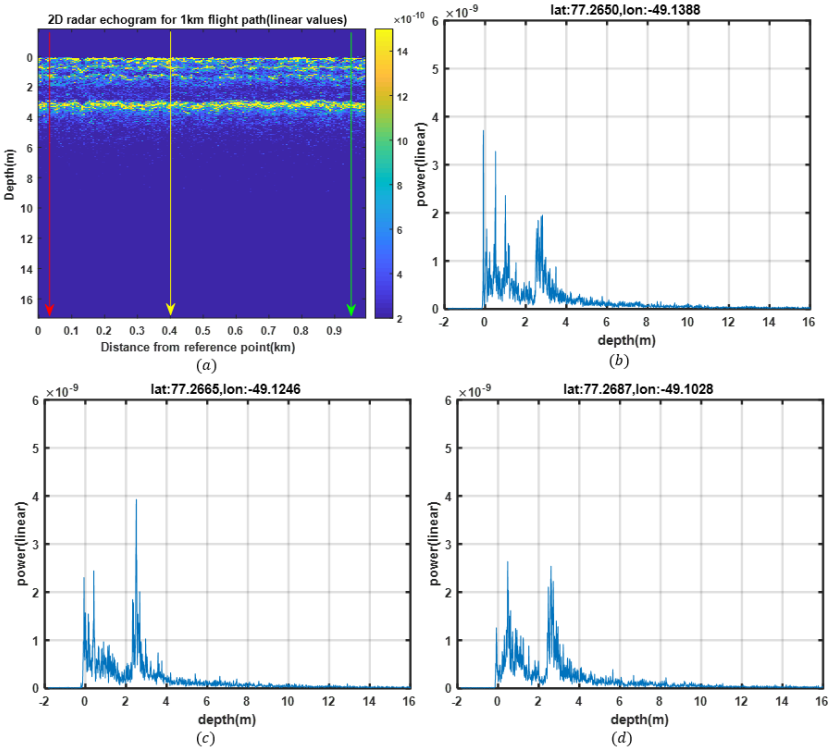

Figure 5 (a) Snow Radar echogram versus depth in the firn along the flight path. (Other plots) Three selected echo profiles from the echogram positions are denoted as red(b) yellow(c) and green(d). The echogram show bright edges near the surface which can be attributed to the refrozen layers with higher dielectric contrast.

Figure 6 and Figure 7 compare CFM simulated density profiles for cross-over locations 1-2 (Figure 5) and 3-4 (Figure 7) with the 1 km averaged radar echoes as a function of depth. All locations show secondary backscatter peaks at depth 2-2.5 m that correspond to peaks in the CFM density profiles. These peaks have amplitude comparable to the snow-air interface, which is likely to be caused due to the refrozen layers created in the melt events starting in the year of 2012. The Snow Radar also observes backscatter peaks at shallower depths that do not correspond to similar density features in the simulated profiles, potentially due to inaccuracies in the climate forcing used for recent periods. Additional smaller backscatter peaks appear at 6-8 m depth that in many cases have matching CFM density peaks, but the lower level of the backscatter returns makes a direct comparison with CFM information more challenging.

Formatted: Font color: Red

Formatted: Font color: Red

Formatted: Font color: Red

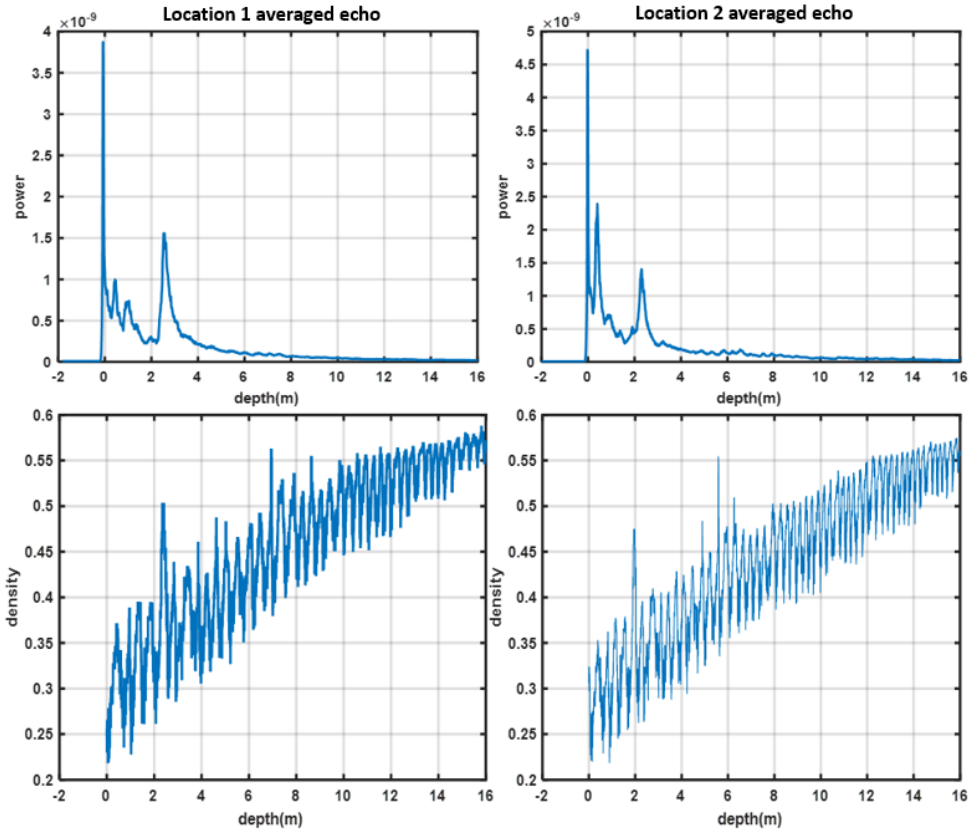

245

Figure 6 Averaged radar echos for cross over points one and two (upper left and right plots) and corresponding CFM simulated density profiles (lower left and right plots)

Formatted: Font color: Red

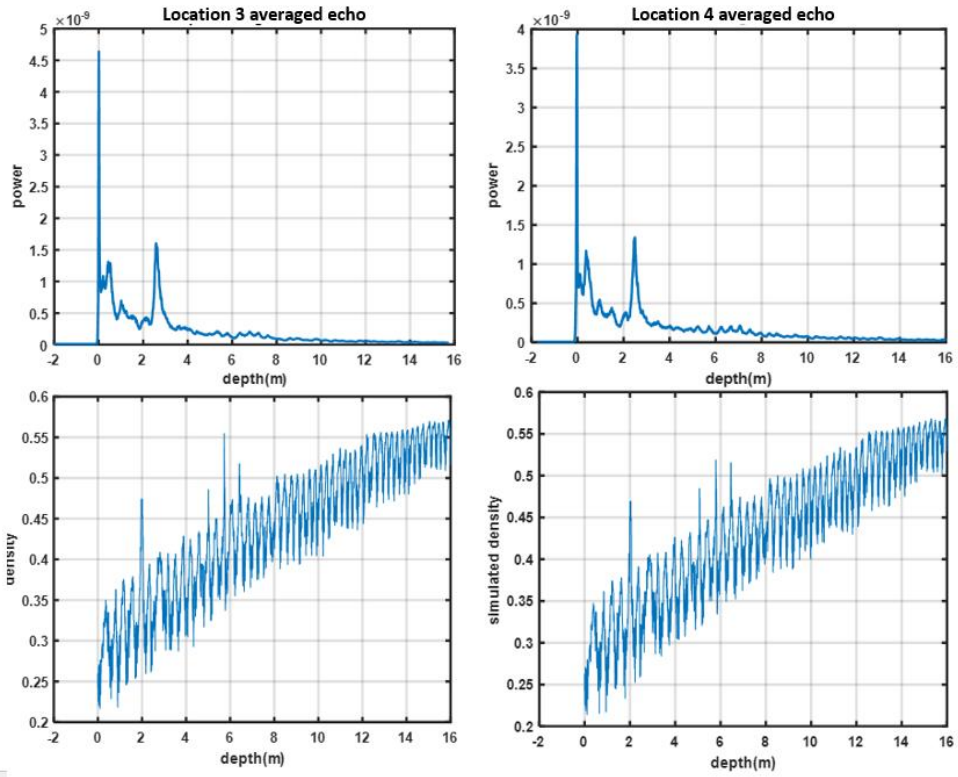

Figure 7~~7~~ Averaged radar echos for cross over points three and two (upper left and right plots) and corresponding CFM simulated density profiles (lower left and right plots)

Formatted: Font color: Red

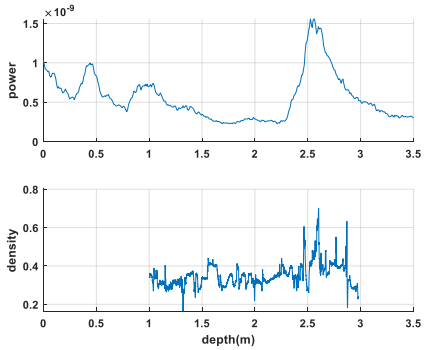

Figure 8 Averaged Snow Radar echo (upper plot) compared to X-ray high resolution tomography density data (lower data) near cross-over site one

2015 X-Ray tomography data providing a snapshot of the upper 2 meters of the firn for a location near cross-over location~~point~~ 1 is shown in Figure 8. The X-ray profile was shifted 1 meter in depth to compensate for snow fall between the 2015 tomography and 2017 radar measurements. The strong radar echo near 2.5m depth again collocates well with X-ray density features near this depth related to the 2012 melt event. It is noted that the tomographic profile corresponds only to a single location rather than the 1 km average used in the radar echo, so that the detailed features in the tomography profile are not observed in the averaged radar measurement, although similar detailed features can be identified in some individual radar echo profiles. Table 4 presents a summary of the numbers of peaks detected in the averaged Snow Radar echogram at each of the four cross-over sites.

	Point1	Point 2	Point 3	Point 4
Number of peaks	3	2	2	2

Table 34: **Peaks in Snow Radar echoes**

The results of this section suggest that strong echoes observed by the Snow Radar are due to refrozen layers in the firn. CFM simulated density peaks are shown to correspond reasonably to high backscatter echoes, with melt event likely happened in the year of 2012. X-Ray tomography data also shows the impact of the 2012 melt event and correlates well with radar measurements[Schaller et al., 2016].

Formatted: Font color: Red

Formatted: Font color: Red

Field Code Changed

Formatted: Font color: Red

Formatted: Font color: Red

3.3. Studies of the impact of each density component on 0.5-2 GHz brightness temperatures

In this section, we use the radiative transfer model to study the frequency response of different component in the firn. The reflection is evaluated for long scale, short scale and the refrozen layers. The model was first applied to simulate the impact of "long scale" density fluctuations on 0.5-2 GHz brightness temperatures. Figure 9:~~Figure 9~~ shows example reflections resulting from long scale firn density variations at the snow-air interface, using the parameter in Table 5. The maximum and minimum

of the reflection within the bandwidth is 0.126 and 0.118, a difference of 0.008. The reflection is unit less as a ratio of reflected power to incident power. The reflectivity is significant but remains approximately constant in frequency in this case.

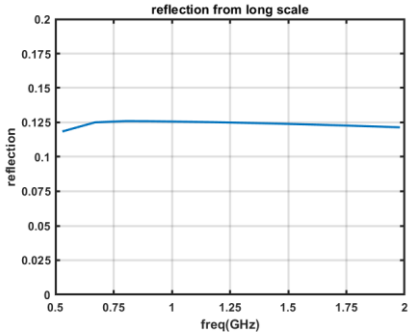

Figure 9: Reflections from the long scale and snow-air interface; the results are almost constant in frequency

A similar study for short scale variations using the parameters in Table 5 is presented in Figure 10: ~~Figure 10~~ . The parameters of the $std(\rho)$ and l_z is from the results of [Tan 2021]. We used a small horizontal correlation length for the short scale since that these kind of small variations are hard to pertain horizontally in the scale of 10s of centimetres. We also assume the short scale exists in a shorter vertical range due to densification effect. The small reflectivity values obtained suggest that the contribution of short scales is negligible compared to the long scale.

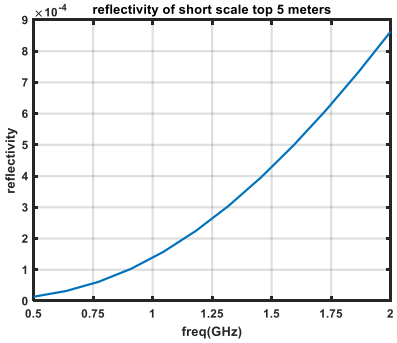

Figure 10: Reflectivity from short scale fluctuations in the top five meters

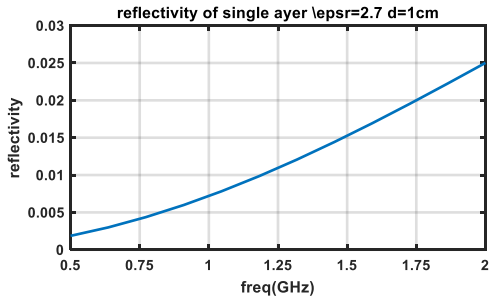

Figure 11: Reflectivity of a single layer with permittivity 2.7 and 1cm thickness in a mean permittivity of $\epsilon_r = 1.63$(0.35g/cm^3 in density)

The reflectivity resulting from a single refrozen layer of relative permittivity 2.7 and 1 cm thickness in a background of relative permittivity 1.63 is shown in Figure 11. These results show a significant variation with frequency, ranging from 0.002 to 0.025 from 0.5 to 2GHz, suggesting that refrozen layers can be important contributors to the frequency variation in 0.5-2 GHz brightness temperatures. Table 5 provides a further summary of insights obtained from Figures 9-11 and other similar simulations.

Scales Deterministic or random 3D or layered measurements	**~~cor~~l_ρ (not modelled, a hypotheses) , l_ρ/l_z**	**$\Delta\rho(g/cm^3)$ ~~cor~~l_z or thickness(cm)**	**Extent in depth**	**Number of reflections**	**Reflections Magnitude (i) each (ii) Total**	**Included in Community Firn Model (CFM)?**
Short scale (random 3D) borehole	$2\ cm$ $\frac{l_\rho}{l_z} = 1$	$0.01\ g/cm^3$ $2\ cm$	5m	250	2.5e-5 0.00625=250x2.5e-5	Not modelled because of small variance and small correlation length
Long scale (random 3D) borehole	23 cm $\frac{l_\rho}{l_z} = 2.3$	$0.05\ g/cm^3$ $10\ cm$	30m	300	5e-4 0.15=300x5e-4	yes
Frozen layers	$l_\rho > 10\lambda$	$0.3 g/cm^3$	2m	3	[0.002~0.025] 0.006~0.075	yes

(deterministic, 1D) From radar echo in time domain		1cm				

Table 45: **Properties of the short scale, long scale variations in density and high-density layers**

With the understanding that the refrozen layers are contributing to the reflection change within the 0.5-2GHz range, we now look at the UWBRAD measurements taken at the 4 locations in Fig.1 Figure 12 plots UWBRAD 0.5, 1.1, and 1.8 GHz brightness temperatures at the four cross-over locations. The frequency variations of brightness temperatures at location one (right most point in Figure 12) are larger than the other three points, which can be related to the number of radar echo peaks at these locations (Table 4).

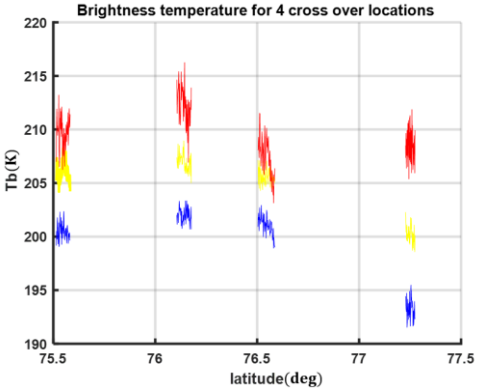

Figure 12: Brightness temperature for 3 channels of 0.5GHz (red), 1.1GHz (yellow) 1.8GHz (blue). Cross-over locations 1 to 4 are from right to left in the figure.

3.4 Comparisons of Modelled and Measured Brightness Temperatures

In this section, the analytical partially coherent model was first used to simulate UWBRAD acquired brightness temperatures. Then the input parameters are compared with the profiles from CFM simulations.

To simulate UWBRAD brightness temperatures, temperature profiles from NGRIP to NEEM retrieved in [Yardim et al 2022] (see Appendix B) are used with the partially coherent model [Tan et al 2021] to provide the upward going brightness temperature at depth $z = -d$. A mean profile of $\rho_m(z) = 0.917 - 0.5748\exp(0.0263z)$ is also used for all four cross-over locations based on analysis of CFM outputs for the 4 locations which were found to have similar mean density behaviours.

Formatted: Font color: Red

Formatted: Font color: Red

Formatted: Font color: Red

An iterative process was used to refine model parameters in order to obtain a reasonable match to the UWBRAD measurements, as shown in Figure 13. It is noted that UWBRAD variations at these sites can be approximately 3K, so that the agreement achieved is comparable to the measurement accuracy.

Table 6 summarizes the parameters obtained; note that $std(\rho)$ and l_z were decreased in depth through a multiplication with the functions $exp(z/33)$ and $exp(z/55)$, respectively where z is the depth in meters, for the large scale and by $exp(z/5)$ for the short scale. Numbers in the exponential functions are in terms of meters. The selection of the exponential decays for the $std(\rho)$ long scale is to make sure that the density fluctuations would disappear when the firn is very close to ice . For short scale, the decay is much faster due to densification, believing the effects are negligible. Decrease of correlation length is a tuning parameter to make sure the $std(\rho)$ becomes 0 before l_z becomes too small$(4k_m'^2 l_z^2 \ll 1)$. The horizontal correlation length for the long scale variations was obtained as $l_\rho = 23cm$, which appears consistent with reports from in-situ investigations and is similar to the properties of firn surface horizontal variations. The permittivity and thickness of the high-density layers used in simulating the brightness temperature are also listed in Table 5~~Table 6~~; the number of high-density layers at each site was selected based on the radar analysis in Table 4.

Formatted: Font color: Red

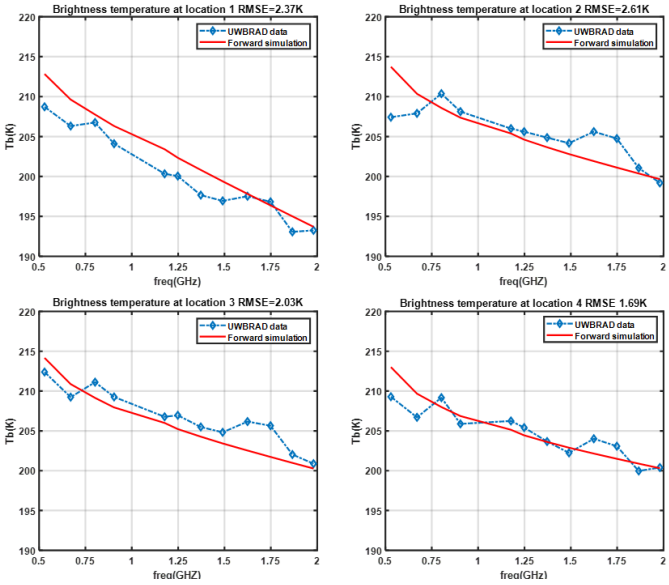

Figure 13: Brightness temperature over the 4 overlapping positions. The simulated results are plotted together with the UWBRAD data

Long scale density fluctuation parameters inferred from the CFM are listed in **Table 6**~~Table 7~~ for comparison. For site one, the microwave estimated $std(\rho)$ is $0.058 g/cm\text{^}3$ with $l_z = 11.5cm$, while the corresponding values for sites two through four are $0.053 g/cm\text{^}3$ with correlation length ~ $9cm$. The CFM results show $std(\rho)$ values of 0.036g/cm^3 with $l_z = 10.5cm$ for Pt1 and $0.033 g/cm\text{^}3$ with vertical correlation length close to 7cm for the other sites. While the $std(\rho)$ used in the forward model is about 0.02g/cm^3 higher than the CFM, $std(\rho)$ values in both cases agree in the higher $std(\rho)$ and l_z values at location 1. While differences in the microwave-derived and CFM derived density fluctuation values are significant, the relative agreement achieved suggests that 0.5-2 GHz brightness temperatures can provide information on firn density fluctuations if refrozen layer effects are accounted for using radar-derived information.

		Pt1	Pt2	Pt3	Pt4
Long scale	$std(\rho)(z = 0)$(g/cm^3)	0.058	0.053	0.053	0.054
	$l_z(z = 0)(cm)$	11.5	9.1	9.3	9.2
Refrozen layers	Permittivity	2.6;2.7;2.7	2.6;2.7	2.6;2.7;	2.6;2.6
	Thickness (cm)	0.9,1.1,1.1	0.95,0.9	0.95,0.9	0.85,0.9

Table 5~~6~~: Parameters used in forward modelling brightness temperature, the decrease of $\boldsymbol{std(\rho)}$ and $\boldsymbol{l_z(z)}$ follows $\boldsymbol{exp(z/33)}$

	Pt1	Pt2	Pt3	Pt4
$std(\rho)$(g/cm^3)	0.036	0.033	0.0325	0.0325
l_z(cm)	10.5	6.2	7.14	7.2
Accumulation (m i.e. yr^{-1})	0.293	0.148	0.148	0.193

Table 6~~7~~: Near surface long scale properties from CFM simulation and Accumulation rate

4. Discussion

Modelling the density fluctuations with horizontal variation on the scale of wave length enables the coupling between emission of V and H polarized brightness temperature. To show this effects, we compare the forward modelling results using finite l_ρ and $l_\rho = \infty$ with SMOS data collected over Dome C, Antarctica where in-situ studies have been performed [Brogioni et al 2015]. [Leduc-Leballeur etal 2015]; The V and H polarized brightness temperature was modelled in [Tan etal 2015], however the 1D random media model could not explain the H polaried TB.

Forward model predictions were also compared with brightness temperatures at Dome C measured by the SMOS satellite. SMOS operates at 1.4 GHz and has both V and H channels. The synthetic aperture technique in SMOS make multi-angle observations possible as provided in the SMOS L1C data product. Firn properties at DOME C are very different from those in

Formatted: Font color: Red
Formatted: Font color: Red
Formatted: Font color: Red
Formatted: Font color: Red
Formatted: Font color: Red
Formatted: Font color: Red

Greenland. The accumulation rate of Dome C is 0.1m/year [Brogioni et al 2015] in contrast to the higher accumulation rates in Greenland shown in Table 6~~Table 7~~. A shorter correlation length therefore should be expected as compared to Greenland, and temporal effects on the firn will less significant compared to Greenland. Refrozen layers at this site are also neglected as significant melt events are not expected. A comparison of the firn properties used in Greenland and at Dome C is provided in Table 7~~Table 8~~ to summarize these discussions.

Scales	Greenland	Dome C
Short scale(z=0)	$0.01 g/cm^3, l_z = 2cm, l_\rho = 2cm$	No short scale
Long scale(z=0)	$0.05 g/cm^3, l_z = 10cm,$ $l_\rho = 23cm, \frac{l_\rho}{l_z} = 2.3$	$0.053 g/cm^3$, $l_z = 8.2cm$, $l_\rho = 10cm$
Frozen layers	$0.3 g/cm^3$ 1cm thick, $l_\rho > 10\lambda$ 3 layers,	No Frozen layers

Table 7~~8~~: **Firn properties in Greenland and at Dome C**

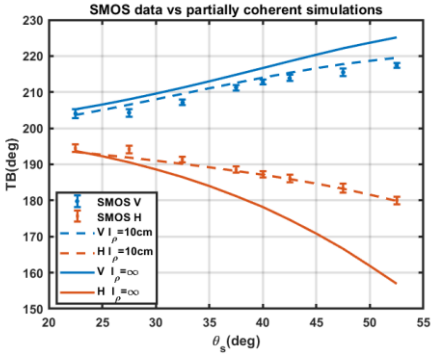

Figure 14: 10 year averaged SMOS data compared with partially coherent model forward simulations

Forward model predictions of 1.4 GHz brightness temperatures versus angle are shown in Figure 14 using $l_\rho = 10cm$ and $l_\rho = \infty$, along with SMOS measurements averaged over a 10-year time period from 2011 to 2021. The SMOS error bars further indicate the expected accuracies of the SMOS data shown.

In simulating the results, the density parameters at z=0 are given by Table 7~~Table 8~~. The surface density fluctuation is selected between the ground measurements data at Dome C [Brogioni et al 2015] and the values obtained in [Leduc-Leballeur etal

Formatted: Font color: Red

Formatted: Font: (Asian) +Body Asian (SimSun), Not Bold, (Asian) Chinese (PRC)

Formatted: Font: (Asian) +Body Asian (SimSun), Not Bold, Font color: Black, (Asian) Chinese (PRC), Check spelling and grammar

Formatted: Font color: Red

Formatted: Font color: Red

Formatted: Font color: Red

Formatted: Font color: Red

2015]; note that information on the density correlation length is not provided in these works. The mean profile density follows [Brogioni et al 2015] and a Robin-model temperature model is used. We assume that $std(\rho)$ and l_z have dependence of $\exp(z/30)$ and $\exp(z/40)$ respectively to model the process of densification.

The results show that the model predictions with $l_\rho = 10cm$ provide good agreement with SMOS data in the range 22.5- 52.5 degrees incidence angle, and with RMS difference over angle of 1.4K in V and 0.8K in H. The one dimensional $l_\rho = \infty$ results in contrast show up to 17K differences in the H-pol simulations. These results show that including the effects of finite horizontal correlation length allows the coupling between angle and polarization effects necessary to reproduce SMOS observations.

The analysis of UWBRAD data over Greenland and Dome-C Antarctica have shown the strong effects of density fluctuations over the brightness temperature in L band. This shows that passive microwave can be used as a tool to infer the density fluctuations remotely. Previously, density properties can only be obtained by in-situ measurements (e.g. snow pit), which can only be taken over several places for a given period of time in a year. Characterizing the density fluctuation change can help charactering the mass balance of firn given that the elevation change of firn can be due to the density change.

The radiative transfer model developed here can also be used to analyse the time series brightness temperature over the regions where perennial firn aquifer exists. Resolution enhanced time series brightness temperature collected by SMAP over these regions has shown an exponential like pattern from the end of melting season to the early Spring of the next year [Miller etal 2020 Miller etal 2018]. Physical modelling work for the V and H TB data from SMAP has been performed by [Alexandra 2016], but the forward modelled results show a much larger TB difference in the V an H channels. Based on the model in this paper, we can try to better interpret the SMAP observations physically.

As in the previous studies, density fluctuations have also affected the retrieval of temperature profiles of the ice sheet. The retrieval can be improved by knowing the density better.

Conclusions

The results of the paper suggest a combined active and passive method for sensing long scale fluctuations in the firn density. These fluctuations contain information on accumulation and densification within the firn. The Community Firn Model was used to generate profiles for comparison, and was shown to produce simulated profiles having reasonable agreement with in situ measurements provided that appropriate high resolution forcing data was available. Snow Radar echo measurements were shown to provide information on refrozen layers within the firn, that could then be accounted for in analyzing 0.5-2 GHz brightness temperature datasets. The analytical partially coherent model reported was found to provide reasonable agreement with measured 0.5-2 GHz brightness temperatures by including the effects of refrozen layers and long scale density fluctuations. Comparisons with SMOS measurements at Dome-C in particular demonstrate the coupling between H and V polarizations that

is captured by the continuous random medium description used in the model. This work shows that the co-located active and passive microwave data can be used to infer the polar firn properties that can further be compared with predictions of CFM.

Appendix A First order iterative approach for firn emission

In this appendix, we give the details of the first order solution of radiative transfer equations with a varying mean and fluctuating profile. The density profile is defined by:

$$\rho(z) = \rho_m(z) + \rho_f(z)$$

Where $\rho_m(z)$ is the mean profile which increases as the depth increases,$\rho_f(z)$ is the fluctuating profile with the standard deviation $std(\rho_f)(z)$ and vertical correlation length $l_z(z)$ decreases as z decreases. The radiative transfer equations for the density fluctuating region is given as:

$$cos\theta \frac{\mathrm{d}}{\mathrm{dz}} \vec{I}_u(\theta, z) = -\kappa_a(z)\vec{I}_u(\theta, z) + \kappa_a(z)CT_0 - \kappa_s(\theta, z)\vec{I}_u(\theta, z) + \int_0^{\frac{\pi}{2}} sin\theta' P_{uu}(\theta, \theta', z)\, \vec{I}_u(\theta', z) + \int_0^{\frac{\pi}{2}} sin\theta' P_{du}(\theta, \theta', z)\, \vec{I}_d(\theta', z)$$

And

$$-cos\theta \frac{\mathrm{d}}{\mathrm{dz}} \vec{I}_d(\theta, z) = -\kappa_a(z)\vec{I}_d(\theta, z) + \kappa_a(z)CT_0 - \kappa_s(\theta, z)\vec{I}_d(\theta, z) + \int_0^{\frac{\pi}{2}} sin\theta' P_{ud}(\theta, \theta', z)\, \vec{I}_u(\theta', z) + \int_0^{\frac{\pi}{2}} sin\theta' P_{dd}(\theta, \theta', z)\, \vec{I}_d(\theta', z)$$

The boundary conditions are given as the following:

$$\vec{I}_d(\theta, z = 0) = \vec{r}_{10}(\theta)\vec{I}_u(\theta, z = 0)$$

And

$$\vec{I}_u(\theta, z = -d) = CT_2$$

The intensity vectors contains the first and second components of the stokes vector. In the region we consider, which is about tens of meters below the surface, the physical temperature of the firn is almost a constant number, T_0.

The expressions for the phase functions can be found in [Tsang 2001].To find the solution, we multiply $\exp(-\int_{z'}^{0} \kappa_a(z'')sec\theta dz'')$ to the equation of upward going intensity and integrate the equation from $z' = -d$ to $z' = z$,after some math manipulations, we have the expressions for upward as:

$$\vec{I}_u(\theta,z) = CT_2 \exp\left(-\int_{-d}^{0}\kappa_a(z'')sec\theta dz''\right) + sec\theta\int_{-d}^{z} dz'\kappa_a(z')CT_0\exp(-\int_{z'}^{z}\kappa_a(z'')sec\theta dz'')$$

$$- sec\theta\int_{-d}^{z} dz'\kappa_s(\theta,z')\vec{I}_u(\theta,z')\exp\left(-\int_{z'}^{z}\kappa_a(z'')sec\theta dz''\right)$$

$$+\int_{-d}^{z} dz'\exp(-\int_{z'}^{z}\kappa_a(z'')sec\theta dz''\left[\int_0^{\frac{\pi}{2}} P_{uu}(\theta,\theta',z')\vec{I}_u(\theta',z') + \int_0^{\frac{\pi}{2}} P_{du}(\theta,\theta',z')\vec{I}_d(\theta',z')\right]$$

for the downward intensity, we multiply the downward equation with $\exp(-\int_{-d}^{z'}\kappa_a(z'')sec\theta dz'')$ and integrate from $z' = z$ to $z' = 0$. The downward intensity is then obtained as:

$$\vec{I}_d(\theta,z) = \overleftrightarrow{r}_{10}(\theta)CT_2\exp\left(-\int_{-d}^{0}\kappa_a(z'')sec\theta dz''\right)\exp\left(-\int_{z}^{0}\kappa_a(z'')sec\theta dz''\right)$$

$$+\overleftrightarrow{r}_{10}(\theta)\exp\left(-\int_{z}^{0}\kappa_a(z'')sec\theta dz''\right)sec\theta\int_{-d}^{0} dz'\kappa_a(z')CT_0\exp(-\int_{z'}^{0}\kappa_a(z'')sec\theta dz'')$$

$$+ sec\theta\int_{z}^{0}\kappa_a(z')CT_0\exp(-\int_{z}^{z'}\kappa_a(z'')sec\theta dz'')dz'$$

$$-\overleftrightarrow{r}_{10}(\theta)\exp\left(-\int_{z}^{0}\kappa_a(z'')sec\theta dz''\right)sec\theta\int_{-d}^{0} dz'\kappa_s(\theta,z')\vec{I}_u(\theta,z')\exp\left(-\int_{z'}^{0}\kappa_a(z'')sec\theta dz''\right)$$

$$+\overleftrightarrow{r}_{10}(\theta)\exp\left(-\int_{z}^{0}\kappa_a(z'')sec\theta dz''\right)sec\theta\int_{-d}^{0} dz'\exp(-\int_{-d}^{0} dz'\kappa_a(z')sec\theta dz')\left[\int_0^{\frac{\pi}{2}} sin\theta' P_{uu}(\theta,\theta',z')\vec{I}_u(\theta',z')\right.$$

$$\left.+\int_0^{\frac{\pi}{2}} sin\theta' P_{du}(\theta,\theta',z')\,\vec{I}_d(\theta',z')\right]$$

$$-sec\theta\int_{z}^{0}\kappa_s(\theta,z')\vec{I}_d(\theta,z')\exp\left(-\int_{z}^{z'}\kappa_a(z'')sec\theta dz''\right)dz'$$

$$+sec\theta\int_{z}^{0}\exp(-\int_{z}^{z'}\kappa_a(z'')sec\theta dz'')\left[\int_0^{\frac{\pi}{2}} sin\theta' P_{ud}(\theta,\theta',z')\vec{I}_u(\theta',z') + \int_0^{\frac{\pi}{2}} sin\theta' P_{ud}(\theta,\theta',z')\vec{I}_d(\theta',z')\right]$$

The zeroth order solution for the upward and downward intensities are given as:

$$\vec{I}_u^{(0)}(\theta,z) = CT_2\exp\left(-\int_{-d}^{0}\kappa_a(z'')sec\theta dz''\right) + sec\theta\int_{-d}^{z} dz'\kappa_a(z')CT_0\exp(-\int_{z'}^{z}\kappa_a(z'')sec\theta dz'')$$

And

$$\vec{I}_d^{(0)}(\theta,z) = \overleftarrow{r}_{10}(\theta)CT_2 \exp\left(-\int_{-d}^{0}\kappa_a(z'')sec\theta dz''\right)\exp\left(-\int_{z}^{0}\kappa_a(z'')sec\theta dz''\right)$$
$$+\overleftarrow{r}_{10}(\theta)\exp\left(-\int_{z}^{0}\kappa_a(z'')sec\theta dz''\right)sec\theta\int_{-d}^{0}dz'\kappa_a(z')CT_0\exp(-\int_{z'}^{0}\kappa_a(z'')sec\theta dz'')$$
$$+sec\theta\int_{z}^{0}\kappa_a(z')CT_0\exp(-\int_{z}^{z'}\kappa_a(z'')sec\theta dz'')dz'$$

The first order solution of the upward intensity is given as

$$\vec{I}_u^{(1)}(\theta,z) = -sec\theta\int_{-d}^{z}dz'\kappa_s(\theta,z')\vec{I}_u^{(0)}(\theta,z')\exp\left(-\int_{z'}^{z}\kappa_a(z'')sec\theta dz''\right)$$
$$+sec\theta\int_{-d}^{0}dz'\exp(-\int_{z'}^{0}\kappa_a(z'')sec\theta dz'')\left[\int_{0}^{\frac{\pi}{2}}sin\theta' P_{uu}(\theta,\theta',z')\vec{I}_u(\theta',z')\right.$$
$$\left.+\int_{0}^{\frac{\pi}{2}}sin\theta' P_{du}(\theta,\theta',z')\vec{I}_d(\theta',z')\right]$$

The specific intensity at $z = 0$ is then given as:

$$\vec{I}_u(\theta,z=0) = \vec{I}_u^{(0)}(\theta,z=0) + \vec{I}_u^{(1)}(\theta,z=0)$$

Appendix B Robin model parameters for the 4 locations

In this Appendix, present the robin model input parameters for the 4 locations

	Total ice thickness	Surface Temp	M	G
Pt1	2656	242.5	0.38	0.0886
Pt2	3155	241.9	0.21	0.06
Pt3	2951	241.5	0.235	0.095
Pt4	3045	241.3	0.295	0.095

Data availability

The Morris density data can be provided upon request. UWBRAD data can be accessed from UWBRAD website.

Author Contributions

Haokui Xu did the major work. Brooke Medley provided all the simulations of density profiles and the map showing data positions over Greenland. Leung Tsang advised on the modelling. Joel.T.Johnson and Kenneth .C.Jezek provided UWBRAD

data and valuable comments on the paper. Macro Brogioni, and Lars Kaleschke provide the SMOS data over Dome C and suggested the usage of data.

Competing interests

The authors declare that they have no conflict of interest.

References

M. Andrews *et al.*, "The Ultra-Wideband Software Defined Microwave Radiometer (UWBRAD) for Ice sheet subsurface temperature sensing: Calibration and campaign results," *2017 IEEE International Geoscience and Remote Sensing Symposium (IGARSS)*, Fort Worth, TX, USA, 2017, pp. 237-240, doi: 10.1109/IGARSS.2017.8126938.

Brogioni, Marco., G. Macelloni, F. Montomoli and K. C. Jezek, "Simulating Multifrequency Ground-Based Radiometric Measurements at Dome C—Antarctica," in *IEEE Journal of Selected Topics in Applied Earth Observations and Remote Sensing*, vol. 8, no. 9, pp. 4405-4417, Sept. 2015, doi: 10.1109/JSTARS.2015.2427512.

Brucker, L., Picard, G., & Fily, M. (2010). Snow grain-size profiles deduced from microwave snow emissivities in Antarctica. Journal of Glaciology, 56(197), 514-526.

Champollion, N., Picard, G., Arnaud, L., Lefebvre, E., & Fily, M. (2013). Hoar crystal development and disappearance at Dome C, Antarctica: observation by near-infrared photography and passive microwave satellite. Cryosphere Discussions, 7(1).

CReSIS. 2021. Snow radar Data, Lawrence, Kansas, USA. Digital Media. http://data.cresis.ku.edu/.

Fausto, R. S., Box, J. E., Vandecrux, B., Van As, D., Steffen, K., MacFerrin, M. J., Machguth, H., Colgan, W., Koenig, L. S., and McGrath, D.: A snow density dataset for improving surface boundary conditions in Greenland ice sheet firn modeling, Front. Earth Sci., 6, 51, 2018.

Gelaro, R., McCarty, W., Suárez, M. J., Todling, R., Molod, A., Takacs, L., Randles, C. A., Darmenov, A., Bosilovich, M. G., and Reichle, R.: The modern-era retrospective analysis for research and applications, version 2 (MERRA-2), J. Clim., 30, 5419–5454, 2017.

Jezek, K. C., P. Gogineni and M. Shanableh,., "Radar Measurements of Melt Zones on the Greenland Ice Sheet," Geophysical Research Letters, 21(1), 33-36. 1994

Formatted: Font color: Red

Jezek K C et al., “500–2000-MHz Brightness Temperature Spectra of the Northwestern Greenland Ice Sheet,” IEEE Trans. Geosci. Remote Sens., vol. 56, no. 3, pp. 1485-1496, March 2018.

Jezek, Kenneth C. and Johnson, Joel T. and Drinkwater, Mark R. and Macelloni, Giovanni and Tsang, Leung and Aksoy, Mustafa and Durand, Michael "Radiometric Approach for Estimating Relative Changes in Intraglacier Average Temperature," in *IEEE Transactions on Geoscience and Remote Sensing*, vol. 53, no. 1, pp. 134-143, Jan. 2015, doi: 10.1109/TGRS.2014.2319265.

Koenig, L. S., Steig, E. J., Winebrenner, D. P., & Shuman, C. A. (2007). A link between microwave extinction length, firn thermal diffusivity, and accumulation rate in West Antarctica. Journal of Geophysical Research: Earth Surface, 112(F3).

Koenig, L. S., Ivanoff, A., Alexander, P. M., MacGregor, J. A., Fettweis, X., Panzer, B., ... & Tedesco, M. (2016). Annual Greenland accumulation rates (2009–2012) from airborne snow radar. The Cryosphere.

Leduc-Leballeur., M. *et al*., "Modeling L-Band Brightness Temperature at Dome C in Antarctica and Comparison With SMOS Observations," in *IEEE Transactions on Geoscience and Remote Sensing*, vol. 53, no. 7, pp. 4022-4032, July 2015, doi: 10.1109/TGRS.2015.2388790.

Lewis ,C., “Airborne UHF radar for fine resolution mapping of near surface accumulation layers in Greenland and West Antarctica,” Dept.Elect. Eng. Comput. Sci., M.S. thesis, Univ. Kansas, Lawrence, KS, USA, Dec. 2010.

Li, J., & Zwally, H. J. (2011). Modeling of firn compaction for estimating ice-sheet mass change from observed ice-sheet elevation change. Annals of Glaciology, 52(59), 1-7.

Ligtenberg, S. R. M., Helsen, M. M., & Van den Broeke, M. R. (2011). An improved semi-empirical model for the densification of Antarctic firn. The Cryosphere, 5, 809-819.

Medley, B., Ligtenberg, S. R. M., Joughin, I., Van den Broeke, M. R., Gogineni, S., & Nowicki, S. (2015). Antarctic firn compaction rates from repeat-track airborne radar data: I. Methods. Annals of Glaciology, 56(70), 155-166.

Medley, B., Joughin, I., Das, S. B., Steig, E. J., Conway, H., Gogineni, S., ... & Lenaerts, J. T. (2013). Airborne‐radar and ice‐core observations of annual snow accumulation over Thwaites Glacier, West Antarctica confirm the spatiotemporal variability of global and regional atmospheric models. Geophysical Research Letters, 40(14), 3649-3654.

Medley, B., Joughin, I., Smith, B. E., Das, S. B., Steig, E. J., Conway, H., ... & van den Broeke, M. R. (2014). Constraining the recent mass balance of Pine Island and Thwaites glaciers, West Antarctica, with airborne observations of snow accumulation. The Cryosphere, 8, 1375-1392.

Medley, B., Neumann, T. A., Zwally, H. J., Smith, B. E., & Stevens, C.M.. Forty-year simulations of firn processes over the Greenland and Antarctic ice sheets. The Cryosphere Discussions, 1-35, in Review.

Montgomery, L., Koenig, L., & Alexander, P. (2018). The SUMup dataset: Compiled measurements of surface mass balance components over ice sheets and sea ice with analysis over Greenland, Earth Syst. Sci. Data, 10, 1959–1985.

Morris, E. M., and D. J. Wingham, 2011. The effect of fluctuations in surface density, accumulation and compaction on elevation change rates along the EGIG line, central Greenland. J. Glaciology, vol., 57, no. 203. p. 416-430.

Munneke, P. Kuipers, Ligtenberg, S. R. M., Noël, B. P. Y., Howat, I. M., Box, J. E., Mosley-Thompson, E., ... & Van Den Broeke, M. R. (2015). Elevation change of the Greenland Ice Sheet due to surface mass balance and firn processes, 1960–2014. The Cryosphere, 9(6), 2009-2025.

Jan Baker. 2012. NEEM Firn Core 2009S2 Density and Permeability.https://arcticdata.io/catalog/view/doi:10.18739/A2Q88G

NEGISdensity:https://www1.ncdc.noaa.gov/pub/data/paleo/icecore/greenland/negis2012dens.txt

B. Panzer, C. Leuschen, A. Patel, T. Markus and S. Gogineni, "Ultra-wideband radar measurements of snow thickness over sea ice," 2010 IEEE International Geoscience and Remote Sensing Symposium, Honolulu, HI, USA, 2010, pp. 3130-3133, doi: 10.1109/IGARSS.2010.5654342.

Schaller, C. F., Freitag, J., Kipfstuhl, S., Laepple, T., Steen-Larsen, H. C., and Eisen, O.: A representative density profile of the North Greenland snowpack, The Cryosphere, 10, 1991–2002, https://doi.org/10.5194/tc-10-1991-2016, 2016.

Shepherd, A., Gilbert, L., Muir, A. S., Konrad, H., McMillan, M., Slater, T., ... & Engdahl, M. E. (2019). Trends in Antarctic Ice Sheet elevation and mass. Geophysical Research Letters, 46(14), 8174-8183.

Smith, B., Fricker, H. A., Gardner, A. S., Medley, B., Nilsson, J., Paolo, F. S., ... & Harbeck, K. (2020). Pervasive ice sheet mass loss reflects competing ocean and atmosphere processes. Science, 368(6496), 1239-1242.

Stevens, M., Vo, H., Emmakahle, and Jboat: UWGlaciology/CommunityFirnModel: Version 1.1.6, Zenodo, https://doi.org/10.5281/ZENODO.5719748, 2021.

Tan S. , M. Aksoy, M. Brogioni, G. Macelloni, M. Durand, K. C. Jezek, T.-L. Wang, L. Tsang, J. T. Johnson, M. R. Drinkwater, and L. Brucker, “Physical Models of Layered Polar Firn Brightness Temperatures

Formatted: Font color: Red

Formatted: Font: (Default) Times New Roman, (Asian) Times New Roman, 11.5 pt, Font color: Red, English (United Kingdom)

Formatted: Font color: Red

From 0.5 to 2 GHz," IEEE J. Sel. Topics Appl. Earth Observ. Remote Sens., vol. 8, no. 7, pp. 3681-3691, July 2015.

Tan S etal , "A Partially Coherent Approach for Modeling Polar Ice Sheet 0.5–2-GHz Thermal Emission," in IEEE Transactions on Geoscience and Remote Sensing, vol. 59, no. 10, pp. 8062-8072, Oct. 2021, doi: 10.1109/TGRS.2020.3039057.

Tsang, L., J.A. Kong, and K.H. Ding (2000), Scattering of Electromagnetic Waves, Vol. 1: Theory and Applications, Wiley Interscience, 2000, 426 pages

Vallelonga etal Initial results from geophysical surveys and shallow coring of the Northeast Greenland Ice Stream (NEGIS),The Cryosphere, 2014

Wuite, J., and K.C.Jezek, Investigations of the upper snow pack at NGRIP, Greenland, Project report.

C. Yardim et al., "Greenland Ice Sheet Subsurface Temperature Estimation Using Ultrawideband Microwave Radiometry," in IEEE Transactions on Geoscience and Remote Sensing, vol. 60, pp. 1-12, 2022, Art no. 4300312, doi: 10.1109/TGRS.2020.3043954.

Zabel, I.H.H., K.C. Jezek, P.A. Baggeroer and S.P. Gogineni. Radar Observations of Snow Stratigraphy and Melt Processes on the Greenland Ice Sheet. Annals of Glaciology. vol 21, p. 40-44. 1995

Formatted: Indent: Left: 0", Hanging: 0.5"